



## CSO AND CARMA OBSERVATIONS OF L1157. II. CHEMICAL COMPLEXITY IN THE SHOCKED OUTFLOW

ANDREW M. BURKHARDT<sup>1</sup>, NIKLAUS M. DOLLHOPF<sup>1</sup>, JOANNA F. CORBY<sup>1</sup>, P. BRANDON CARROLL<sup>2</sup>,  
CHRISTOPHER N. SHINGLEDECKER<sup>3</sup>, RYAN A. LOOMIS<sup>4</sup>, SHAWN THOMAS BOOTH<sup>1</sup>, GEOFFREY A. BLAKE<sup>2,5</sup>, ERIC HERBST<sup>1,3</sup>,  
ANTHONY J. REMIJAN<sup>6</sup>, AND BRETT A. MCGUIRE<sup>6,7</sup>

<sup>1</sup> Department of Astronomy, University of Virginia, Charlottesville, VA 22904, USA

<sup>2</sup> Division of Chemistry and Chemical Engineering, California Institute of Technology, Pasadena, CA 91125, USA

<sup>3</sup> Department of Chemistry, University of Virginia, Charlottesville, VA 22904, USA

<sup>4</sup> Department of Astronomy, Harvard University, Cambridge, MA 02138, USA

<sup>5</sup> Division of Geological and Planetary Sciences, California Institute of Technology, Pasadena, CA 91125, USA

<sup>6</sup> National Radio Astronomy Observatory, Charlottesville, VA 22903, USA; [bmcguire@nrao.edu](mailto:bmcguire@nrao.edu)

Received 2016 February 4; revised 2016 May 26; accepted 2016 May 26; published 2016 August 3

## ABSTRACT

L1157, a molecular dark cloud with an embedded Class 0 protostar possessing a bipolar outflow, is an excellent source for studying shock chemistry, including grain-surface chemistry prior to shocks, and post-shock, gas-phase processing. The L1157-B1 and B2 positions experienced shocks at an estimated  $\sim 2000$  and 4000 years ago, respectively. Prior to these shock events, temperatures were too low for most complex organic molecules to undergo thermal desorption. Thus, the shocks should have liberated these molecules from the ice grain-surfaces en masse, evidenced by prior observations of SiO and multiple grain mantle species commonly associated with shocks. Grain species, such as OCS, CH<sub>3</sub>OH, and HNCO, all peak at different positions relative to species that are preferably formed in higher-velocity shocks or repeatedly shocked material, such as SiO and HCN. Here, we present high spatial resolution ( $\sim 3''$ ) maps of CH<sub>3</sub>OH, HNCO, HCN, and HCO<sup>+</sup> in the southern portion of the outflow containing B1 and B2, as observed with Combined Array for Research in Millimeter-Wave Astronomy. The HNCO maps are the first interferometric observations of this species in L1157. The maps show distinct differences in the chemistry within the various shocked regions in L1157B. This is further supported through constraints of the molecular abundances using the non-LTE code RADEX. We find that the east/west chemical differentiation in C2 may be explained by the contrast of the shock's interaction with either cold, pristine material or warm, previously shocked gas, as seen in enhanced HCN abundances. In addition, the enhancement of the HNCO abundance toward the the older shock, B2, suggests the importance of high-temperature O-chemistry in shocked regions.

*Key words:* astrochemistry – ISM: individual objects (L1157) – ISM: molecules

## 1. INTRODUCTION

Shocks and turbulence are prevalent in molecular gas, from dense gas undergoing star formation to diffuse material filling the thin disk of the Galaxy. Thus, it is crucial to understand the underlying chemistry within shocked regions. For many complex molecules, gas-phase formation routes are inefficient under interstellar conditions, and are unable to reproduce observed abundances. Theoretical work instead predicts efficient chemical reactions on the ice mantles of dust grains (Brown et al. 1988; Herbst & van Dishoeck 2009), and laboratory work confirms that grain-surface chemistry efficiently produces diverse molecular species (Garozzo et al. 2010; Palumbo 2015). Low-velocity C-shocks, which are common in dense molecular clouds, sublimate the ice from the surfaces of grains without destroying most molecular bonds (Requena-Torres et al. 2006). As a result, gas-phase observations of recently shocked clouds can provide substantial information on the condensed-phase chemistry that occurred prior to the passage of the shock. Reactions on the surface of grains are now believed to be responsible for the formation of most complex organic species (Garrod 2013), and studies of shocked molecular clouds are essential for understanding the processing of molecular material and the formation of biologically relevant molecules. Given the

difficulties of unambiguously identifying molecules trapped in ice grains, shock-chemistry studies are among the most promising cases for understanding ice grain chemistry.

The nearby ( $\sim 250$  pc) dark cloud, L1157, provides an excellent opportunity to study shock chemistry. L1157 contains a Class 0 protostar, L1157-mm, with a bipolar outflow that extends  $\sim 2'$ , or  $3 \times 10^4$  au, from the central infrared source (Looney et al. 2007). The blueshifted and redshifted outflows are referred to as L1157B and L1157R, respectively. As the jet precesses, the periodic ejection events produce bow shocks at multiple positions in the outflow (Gueth et al. 1996). The bow shocks, in turn, produce regions of minimal protostellar heating of the dust, and significant shock-induced non-thermal desorption of grain mantles (Fontani et al. 2014).

L1157-B1 and B2 are prominent, recently shocked regions in the southern, blueshifted lobe of the outflow. B1 is warmer and more recently shocked ( $T_{\text{kin}} \sim 80\text{--}100$  K,  $t \sim 2000$  years) than B2 ( $T_{\text{kin}} \sim 20\text{--}60$  K,  $t \sim 4000$  years; Tafalla & Bachiller 1995; Gueth et al. 1996; Lefloch et al. 2012). The progenitor gas for B1 and B2 should have had a cold history within the dark cloud (at  $T < 20$  K for  $\sim 1$  Myr). The unshocked portions of the outflow are also cool (at  $T_{\text{kin}} \sim 15\text{--}30$  K; Bachiller et al. 2001). As a result, observations of B1 and B2 primarily probe the chemistry of cold ( $\lesssim 20$  K) ice-grain mantles, and subsequent evolution in the warmer gas-phase.

B1 and B2 are considered chemically active outflows (Bachiller et al. 2001), with the detection of numerous complex

<sup>7</sup> B.A.M. is a Jansky Fellow of the National Radio Astronomy Observatory.

**Table 1**  
Targeted CARMA Transitions

Molecule	Transition	$\nu$ (GHz)	$E_u$ (K)	Beam (arcsec <sup>2</sup> )	rms ( $\sigma$ ) (mJy beam <sup>-1</sup> )
CH <sub>3</sub> OH (methanol)	2 <sub>-1,2</sub> -1 <sub>-1,1</sub>	96.73936(5)	12.9	6''03 × 5''53	8.5
	2 <sub>0,2</sub> -1 <sub>0,1</sub> + +	96.74138(5)	6.9		
	2 <sub>0,2</sub> -1 <sub>0,1</sub>	96.74455(5)	20.1		
	2 <sub>1,1</sub> -1 <sub>1,0</sub>	96.75551(5)	28.0		
HCN (hydrogen cyanide)	$J = 1-0, F = 1-1$	88.63042(2)	4.25	3''45 × 3''27	4.8
	$J = 1-0, F = 2-1$	88.63185(3)	4.25		
	$J = 1-0, F = 0-1$	88.63394(3)	4.25		
HCO <sup>+</sup> (formylium)	$J = 1-0$	89.18853(4)	4.28	3''39 × 3''23	5.1
HNCO (isocyanic acid)	$J = 4_{0,4}-3_{0,3}$	87.92524(8)	10.6	3''50 × 3''28	7.0

**Note.** The resolved quantum numbers and frequencies of each transition are listed. Also included are the synthesized beam sizes and approximate rms levels for each window, where no spectral binning was performed. Transitions and parameters accessible at [www.splatalogue.net](http://www.splatalogue.net) (Remijan et al. 2007). Cataloged at CDMS (Müller et al. 2005), and JPL (Pickett et al. 1998).

species including HCOOCH<sub>3</sub>, HCOOH, CH<sub>3</sub>CHO, NH<sub>2</sub>CHO, C<sub>2</sub>H<sub>5</sub>OH, and CH<sub>3</sub>CN (Arce et al. 2008; Yamaguchi et al. 2011 and references therein). Abundances of shock tracers including SiO, CH<sub>3</sub>OH, and HNCO are particularly enhanced in B1 and B2 as compared to unshocked regions of the outflow. This includes an SiO abundance enhancement of 10<sup>4</sup> compared to unshocked material in the region, which high spatial resolution ( $\sim 2''5$ ) images indicate that the distribution of SiO closely traces the positions of B1 and B2 (Gueth et al. 1998). Furthermore, L1157-B2 has been found to contain the highest abundance of HNCO yet observed in any source in the Galaxy, including an enhanced abundance of 4–11 times compared to hot cores and dense cores in the Galactic Center (Rodríguez-Fernández et al. 2010; Mendoza et al. 2014).

Interferometric images of multiple molecules have demonstrated the clumpy structure of the southern outflow. Previous work by Benedettini et al. (2007) at  $\lambda = 3$  mm mapped transitions of CS, CH<sub>3</sub>OH, HCN, OCS, and <sup>34</sup>SO at  $\theta \sim 3''-6''$  spatial resolution with the Plateau de Bure Interferometer (PdBI). In this work, we present images of 3 mm transitions of HCO<sup>+</sup>, HCN, CH<sub>3</sub>OH, and HNCO observed by the Combined Array for Research in Millimeter-Wave Astronomy (CARMA). While two of the species have been imaged with comparable resolution, this work produces a higher spatial resolution map of HCO<sup>+</sup> and the first interferometric map of HNCO in L1157.

Furthermore, we build upon the work of McGuire et al. (2015; hereafter Paper I) to estimate column densities and abundances of three of the species (CH<sub>3</sub>OH, HCN, and HNCO) in the B1 and B2 clumps.

## 2. OBSERVATIONS

We observed the southern outflow with the CARMA 15-element array at  $\lambda = 3$  mm, targeting the  $J = 1-0$  transitions of HCN and HCO<sup>+</sup>, four  $J = 2_K-1_K$  transitions of CH<sub>3</sub>OH, and the  $J = 4-3$  transition of HNCO, as described in Table 1. A total of 89.3 hr of observations were conducted: 46.7 hr in C-configuration during 2012 August, 23.3 hr in D configuration between 2012 October and November, and 19.3 hr in E-configuration during 2013 May. All observations were

toward a single pointing position at  $\alpha(\text{J2000}) = 20^{\text{h}}39^{\text{m}}07^{\text{s}}.7$ ,  $\delta(\text{J2000}) = 68^{\circ}01'11''.5$ . The 62 MHz bandwidth, 3 bit mode of the CARMA correlator was used, providing 14 non-contiguous windows with 255 channels each, and resulting in 243 kHz ( $\sim 0.7$  km s<sup>-1</sup>) channel resolution.

The data were reduced using the MIRIAD package (Sault et al. 1995) using standard techniques of bandpass, absolute flux, and complex gain calibration. MWC349 and Neptune were used as primary flux calibrators; the bandpass calibrators were 1635+381, 2232+117, 0102+584, 1743-038, 2015+372, and 3C84; and the gain calibrator was 1927+739. Images were generated using the CLEAN algorithm in the MIRIAD package with a Briggs weighting scheme that tended toward natural weighting, resulting in a synthesized beam of  $3''.4 \times 3''.2$  at the center frequency for the majority of the observed transitions. Image analysis was performed in CASA. The targeted transitions and synthesized beam values are shown in Table 1. The synthesized beam of the CH<sub>3</sub>OH maps are about a factor of two larger than the other observed transitions because the CH<sub>3</sub>OH lines were not observed in the most extended configuration used (C-array). While primary beam corrections were not applied, preliminary analysis implied that the ultimate impact of this correction would be minimal, especially for the regions where we perform more in-depth analysis. It should be noted that the sensitivity of the 10-m antennae will be more significantly reduced at the edges of the primary beam in this single pointing.

## 3. RESULTS

### 3.1. Structure

#### 3.1.1. Summary of L1157B Structure

To orient the reader to the structure of the southern, blueshifted outflow, L1157B, we highlight the positions of the shocked clumps with respect to the two cavities, C1 and C2, originally observed in CO (Gueth et al. 1997). Observations of SiO, a prominent shock tracer, reveal large abundances along the structures of the cavities. Figure 1 shows line emission by CH<sub>3</sub>OH and HCO<sup>+</sup> observed by CARMA with the position of the cavities highlighted. The southern-most cavity,

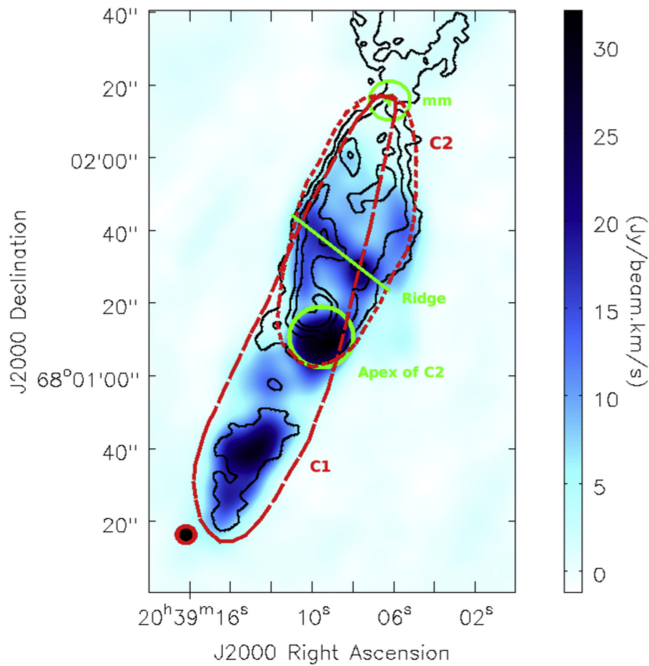


**Figure 1.** Integrated  $\text{CH}_3\text{OH}$  ( $2_k-1_k$ ) emission raster,  $-17.8$  to  $+14.0$   $\text{km s}^{-1}$ , with integrated emission of  $\text{HCO}^+$  ( $1-0$ ) contours,  $-20.1$  to  $+11.9$   $\text{km s}^{-1}$ , overlaid in black, both observed with CARMA. The contour levels for  $\text{HCO}^+$  are 0.44, 0.88, 1.32, 1.76, 2.2  $\text{Jy beam}^{-1} \text{km s}^{-1}$ . The synthesized beam sizes for  $\text{CH}_3\text{OH}$  and  $\text{HCO}^+$  are shown in red and black, respectively, in the lower left. The two cavities in L1157B are shown and labeled in red, with the ridge and apex of C2 shown and labeled in green.

C1, holds the shocked B2 region, while the B1 region is observed at the apex of the C2 (northern) cavity. The bowshock nature of the outflow is apparent from the U-shaped structure of C2 observed with  $\text{CH}_3\text{OH}$ , other shock tracers, and mid-IR emission (Takami et al. 2010).

The B0 region follows the shape of the C1 cavity north of B1 into the L1157-mm source; however, B0 is not correlated with a shock front, and much of it remains cool ( $T_{\text{kin}} \sim 15-30$  K; Bachiller et al. 2001). The aforementioned U-shaped structure along the C2 walls delineates B0 from the ambient gas. The eastern B0 wall shows higher abundances of SiO and HCN than the western wall (Gómez-Ruiz et al. 2013), perhaps suggesting a pseudo-shock event in the region. There is also a ridge of emission connecting the east and west walls of B0, showing similar abundances to the western wall.

High spatial resolution, interferometric observations of the outflow reveal a clumpy structure within L1157 (Benedettini et al. 2007). Within all three regions, molecules are seen to peak in clumps  $\sim 10''-15''$  in diameter. In B1 and B2, these clumps lie within the shocked regions. In B0, these clumps are well correlated with the eastern wall, western wall, and the emission ridge.

### 3.1.2. Structure Revealed by CARMA Maps

The HCN and  $\text{CH}_3\text{OH}$  transitions presented here were previously imaged by Benedettini et al. (2007) with similar resolutions. Indeed, the structure observed by CARMA agrees with the PdBI images previously published. While discussing the structure in this work, we therefore adopt the naming

**Table 2**  
Region Positions and Sizes

Region	Ellipse Center		Ellipse Parameters		
	R.A. (J2000) ( $^{\text{h}} \text{ } ^{\text{m}} \text{ } ^{\text{s}}$ )	decl. (J2000) ( $^{\circ} \text{ } ' \text{ } ''$ )	R.A. ( $''$ )	decl. ( $''$ )	PA ( $^{\circ}$ )
B0a	20 39 10.4	68 01 38.0	11	11	...
B0b	20 39 05.7	68 01 42.0	14	14	...
B0c	20 39 09.0	68 01 36.0	11	11	...
B0d	20 39 07.7	68 01 28.0	12	12	...
B0e	20 39 10.3	68 01 24.0	12	12	...
B0k	20 39 08.1	68 02 00.4	11	11	...
B0l	20 39 06.4	68 01 54.3	11	11	...
B1a	20 39 10.2	68 01 12.0	11	11	...
B1b	20 39 08.8	68 01 10.0	11	11	...
B2a	20 39 12.6	68 00 40.7	7.5	15.5	50
B2b	20 39 13.8	68 00 26.8	7.5	15.5	50
B2c	20 39 11.8	68 00 58.0	13	13	...
B2d	20 39 14.1	68 00 37.7	5	12	0
mm	20 39 06.2	68 02 15.9	11	11	...

**Note.** Regions based off of Benedettini et al. (2007) and Rodríguez-Fernández et al. (2010), with several new clumps assigned (B0k, B0l, and B2d). For non-circular regions, the semiminor axis, semimajor axis, and position angle of the semimajor axis from straight north are given in that order. L1157-mm source size is likely much smaller, but the region size and shape were chosen for comparison to clumps in outflow.

convention of Benedettini et al. (2007) and further added to by Codella et al. (2009) and Gómez-Ruiz et al. (2013). They defined 10 clumps in B0 (B0a–B0j), 8 clumps in B1 (B1a–B1h), and 3 clumps in B2 (B2a–B2c), based primarily on emission from  $\text{CH}_3\text{OH}$ , HCN,  $\text{CH}_3\text{CN}$ , SiO, and  $\text{H}_2\text{CO}$ . To maintain consistency with previous work, we specify elliptical regions corresponding to the clump positions reported in these papers. While the regions were described as ellipses  $\sim 10''-15''$  in size (Benedettini et al. 2007), we specify the dimensions of the ellipses with major and minor axis lengths determined based on the distributions observed in our images. We also define three new clumps: B0k and B0l using the  $\text{HCO}^+$  emission, and B2d using the HNC emission. The coordinates and dimensions of the regions used are defined in Table 2. Also in Table 2, we list the region used to extract the spectra toward the gas surrounding L1157-mm, whose position was determined by Gueth et al. (1997). While the source size is likely much smaller than the region used, the size and shape were chosen for comparison to clumps in outflow. Figure 2 shows the integrated line emission of  $\text{CH}_3\text{OH}$   $2_k-1_k$ , HCN ( $1-0$ ),  $\text{HCO}^+$  ( $1-0$ ), and HNC ( $4_{0,4}-3_{0,3}$ ), with the elliptical regions overlaid.

### 3.1.3. $\text{CH}_3\text{OH}$

$\text{CH}_3\text{OH}$   $2_k-1_k$  displays a clumpy structure that is consistent with the previous observations by Benedettini et al. (2007). In our newly assigned clumps of B0k, B0l, and B2a, we detect emission, although the clumps are not as prominent in  $\text{CH}_3\text{OH}$  emission as in HNC and  $\text{HCO}^+$ . As has been found in previous observations,  $\text{CH}_3\text{OH}$  emission is generally observed to be brighter on the western side of B1, and has significant emission along the ridge in B0.

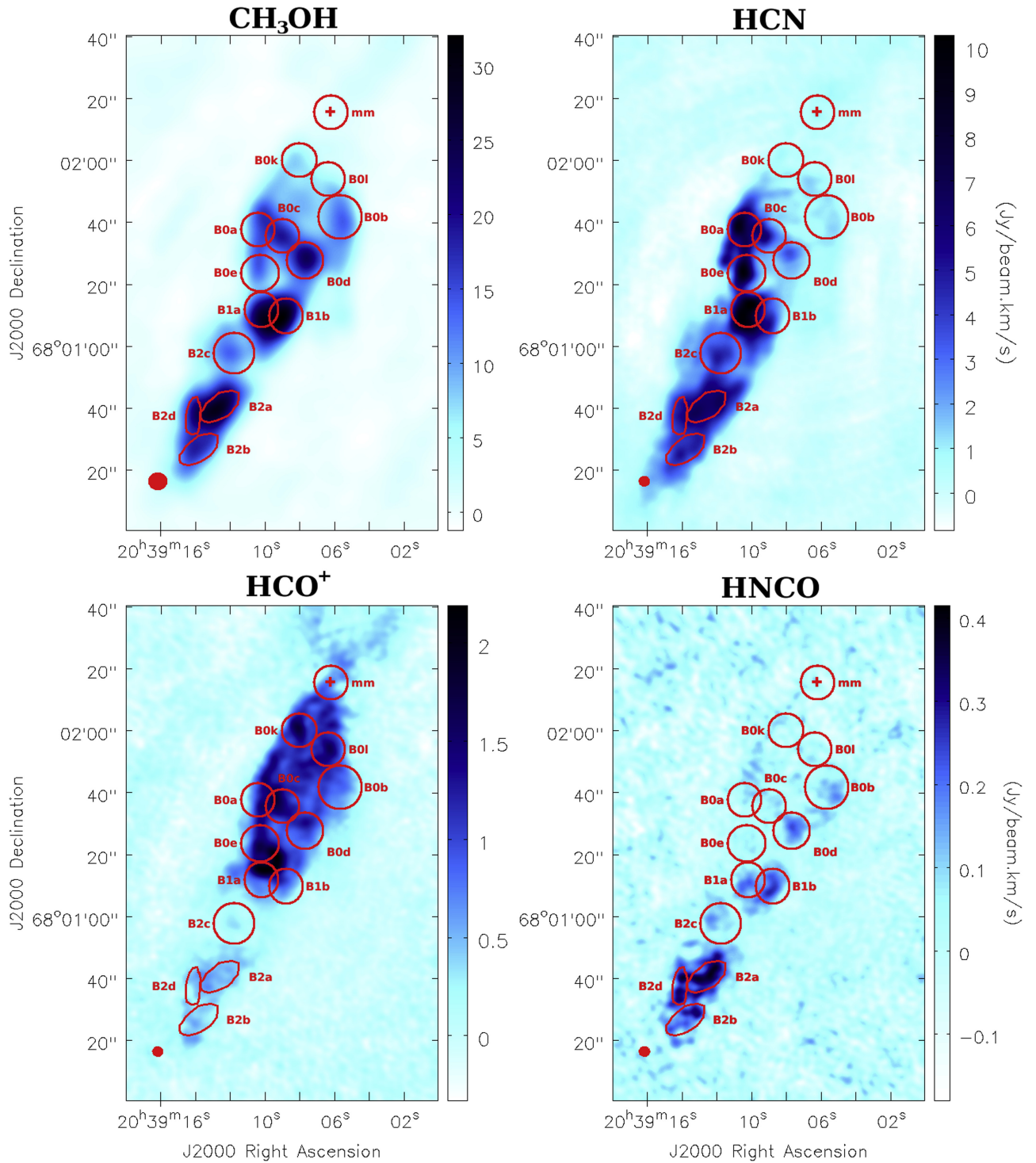


**Figure 2.** Integrated emission maps of  $\text{CH}_3\text{OH}$  ( $2_k-1_k$ ),  $\text{HCN}$  ( $1-0$ ),  $\text{HCO}^+$  ( $1-0$ ), and  $\text{HNCO}$  ( $4_{0,4}-3_{0,3}$ ) with the clump regions and stellar source shown in red. The velocity ranges of integration were  $(-17.8$  to  $+14.0 \text{ km s}^{-1})$ ,  $(-22.1$  to  $+15.0 \text{ km s}^{-1})$ ,  $(-20.1$  to  $+11.9 \text{ km s}^{-1})$ , and  $(-6.45$  to  $+6.9 \text{ km s}^{-1})$ , respectively. The synthesized beam sizes are displayed as filled red in the lower left.

### 3.1.4. HCN

$\text{HCN}$  ( $1-0$ ) shows structure similar to  $\text{CH}_3\text{OH}$ , with significant clumping evident throughout L1157B. However, whereas  $\text{CH}_3\text{OH}$  produces stronger emission on the western wall of the C2 cavity (i.e., in B1b, B0d, B0b),  $\text{HCN}$  emission is strongest on the eastern wall of C2 (i.e., in B1a, B0e, and B0a).

This trend was also reported in Benedettini et al. (2007). Significant structure is also seen outside of these clumps that is not seen in other molecules, especially toward the eastern wall of B0, with an arm protruding to the east of B0. This structure has been observed previously in  $\text{SiO}$  ( $5-4$ ) as an “arc-like” structure to the east of the U-shape of C2 (Gómez-Ruiz

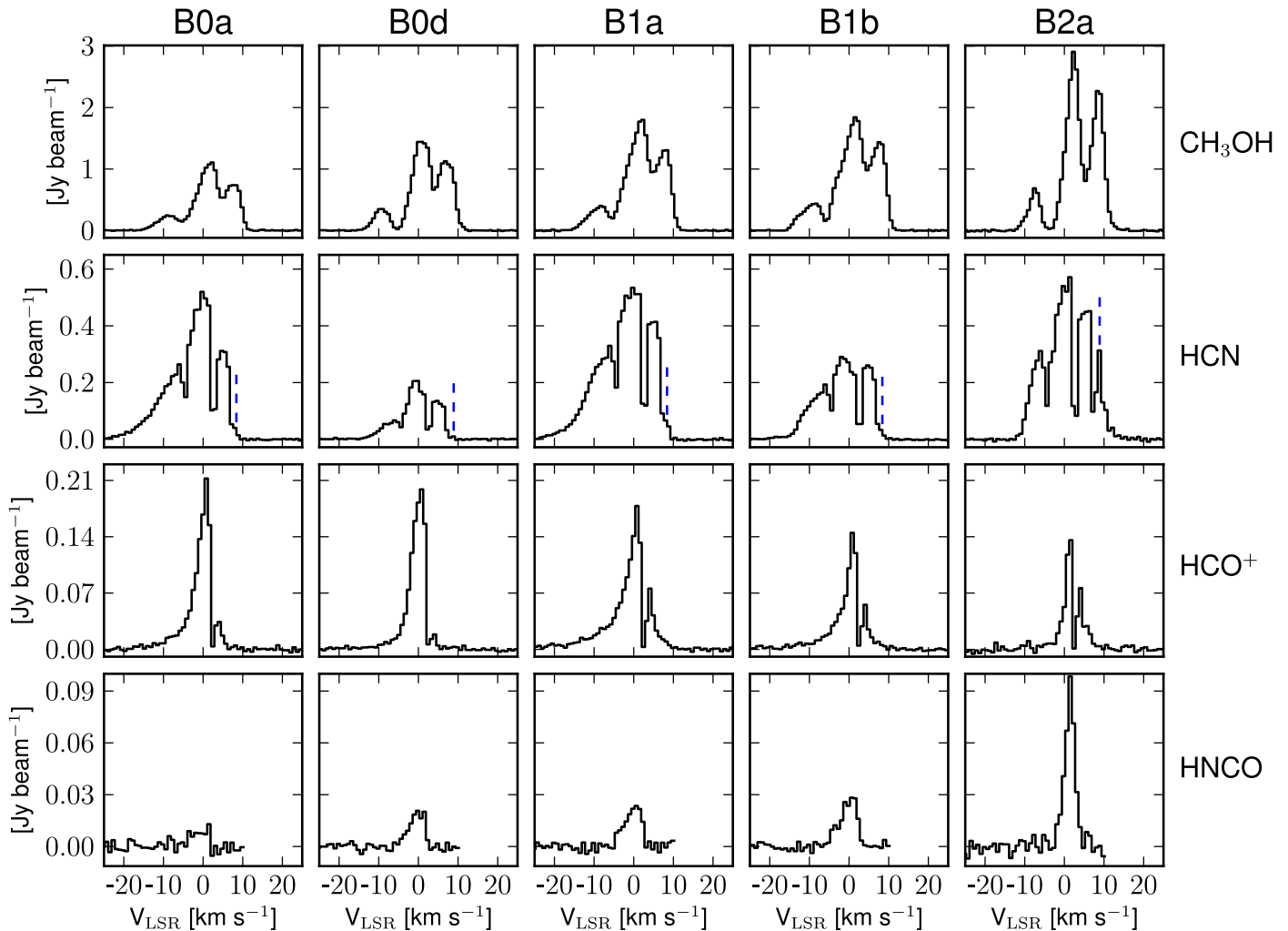


**Figure 3.** The extracted spectra from the regions B0a, B0d, B1a, B1b, and B2a are shown in black. For molecules with multiple transitions, CH<sub>3</sub>OH and HCN, the velocities displayed are relative to the rest frequency of the central transition. For HCN, the unknown feature discussed in Section 3.2.2 is marked with a blue dashed line. Not shown is the transition CH<sub>3</sub>OH 2<sub>1,1</sub>-1<sub>1,0</sub>.

et al. 2013). HCN (1–0) has stronger emission toward the eastern clumps of B1, unlike CH<sub>3</sub>OH, which is consistent with the chemical segregation previously observed (Benedettini et al. 2007). In B2, we observe significant emission toward B2a, B2b, and B2d.

### 3.1.5. HCO<sup>+</sup>

HCO<sup>+</sup> (1–0) exhibits a more extended distribution, and is detected beyond the combined 10–6 m primary beam ( $\sim 2'$ ) of CARMA along the outflow axis. The HCO<sup>+</sup> emission is observed further into B0, tracing the C2 cavity, than the other molecules observed, and extending past the stellar source. We define two new clumps with HCO<sup>+</sup>, B0k and B0l, located in the northern regions near the stellar source, L1157-mm. Strong emission is present in C2, particularly toward the eastern wall and the northern clumps, while much weaker emission is observed toward C1. The distribution is consistent with previous interferometric observations of HCO<sup>+</sup>, where the majority of the emission was observed to trace the low-velocity ambient gas in B0 (Choi et al. 1999; Bachiller et al. 2001).

### 3.1.6. HNC0

HNC0 exhibits a distribution distinct from the other observed species, with significantly stronger line emission from B2. Weaker line emission is associated with B1 and the western wall of B0, similar to CH<sub>3</sub>OH and unlike HCN. Previous single-dish observations have detected strong HNC0 line emission toward B1 and B2, which are in agreement with our observations (Rodríguez-Fernández et al. 2010; Mendoza et al. 2014).

## 3.2. Spectra and Column Density Determination

We extracted spectra from the regions defined in Table 2. Transitions of CH<sub>3</sub>OH, HNC0, and HCN, including hyperfine components, were fit with Gaussian profiles, utilizing a modified version of the line fitting code described in Corby et al. (2015). Figure 3 displays the extracted spectra of the observed molecules at 5 representative regions which probe the emission at a variety of environments across L1157B: B0a, B0d, B1a, B1b, and B2a, with line fits overlaid. Spectra for all

**Table 3**  
Molecular Abundances and Enhancements

	CH <sub>3</sub> OH		HCN			HNCO		
	$N$ (10 <sup>15</sup> cm <sup>-2</sup> )	$\frac{N}{N_{\text{H}_2}}$ (10 <sup>-6</sup> )	$N$ (10 <sup>13</sup> cm <sup>-2</sup> )	$\frac{N}{N_{\text{CH}_3\text{OH}}}$ (10 <sup>-2</sup> )	$\frac{N}{N_{\text{H}_2}}$ (10 <sup>-8</sup> )	$N$ (10 <sup>13</sup> cm <sup>-2</sup> )	$\frac{N}{N_{\text{CH}_3\text{OH}}}$ (10 <sup>-2</sup> )	$\frac{N}{N_{\text{H}_2}}$ (10 <sup>-8</sup> )
B0d	1.5	1.5	2.6	1.7	2.6	2.5	1.6	2.5
B1a	1.9	1.9	10.	5.3	10.	3.2	1.7	3.2
B1b	2.1	2.1	5.3	2.5	5.3	3.8	1.8	3.8
B2a	2.7	2.7	9.9	3.7	9.9	8.0	3.0	8.0
B2b	1.6	1.6	6.6	4.2	6.6	5.5	3.5	5.5
B2d	2.1	2.0	8.0	3.9	7.9	7.5	3.6	7.5

**Note.** For the three molecules studied in depth, the column densities calculated through RADEX are given at each region that coincides with Paper I CSO pointings, along with the enhancement relative to CH<sub>3</sub>OH and overall abundance relative to H<sub>2</sub>. Errors, as described in Paper I, are calculated to be ~32%.

of the defined regions in Table 2 are included in the Appendix A and Gaussian fits parameters are in Appendix B.

An inspection of the line fit parameters reveal the kinematic structure of the outflow. For the purposes of studying the systematic velocities, we use the average velocities for the three strongest components of CH<sub>3</sub>OH and the  $F = 1-1$  hyperfine transition of HCN, which will be further discussed in Sections 3.2.1 and 3.2.2, respectively. The gas surrounding the stellar source, L1157-mm, was found to have velocities between  $v_{\text{LSR}} \sim 2.3-3.1$  km s<sup>-1</sup>. For reference, the cloud velocity for this region has been found to be  $v_{\text{LSR}} \sim 2.6$  km s<sup>-1</sup> (Bachiller & Pérez Gutiérrez 1997).

In general, the clumps located in B0 south of the ridge, B1, and B2c are found to be kinematically related, with average systematic velocities around 0–1.5 km s<sup>-1</sup>. Meanwhile, in the northern part of B0, the systematic velocities generally increase for each species:  $\sim 1$  km s<sup>-1</sup> for CH<sub>3</sub>OH,  $\sim 1.3$  km s<sup>-1</sup> for HCN, and  $\sim 1.6$  km s<sup>-1</sup> for HNCO. Toward B2, the velocities are very consistent and larger than what was found in B1, southern B0, and B2c:  $\sim 2$  km s<sup>-1</sup> for CH<sub>3</sub>OH,  $\sim 0.9$  km s<sup>-1</sup> for HCN, and  $\sim 1.8$  km s<sup>-1</sup> for HNCO. While the line widths of CH<sub>3</sub>OH consistently remain around 3.4 km s<sup>-1</sup> throughout L1157B, HCN has smaller line widths in northern B0 ( $\sim 2.1$  km s<sup>-1</sup>) than the rest of the L1157B, which displays similar line widths to CH<sub>3</sub>OH of  $\sim 3.5$  km s<sup>-1</sup>. Even more dramatically, the line widths of HNCO within these three kinematic regions are found to be distinct:  $\sim 1$  km s<sup>-1</sup> in northern B0,  $\sim 5$  km s<sup>-1</sup> in southern B0 and in B1, and  $\sim 3$  km s<sup>-1</sup> in B2. Curiously, while the HNCO (4–3) line velocity shift in B2c is more related to the apex of C2, the line width is closer to the rest of B2. It is important to note that the current naming scheme for clumps in L1157 does not appear to accurately reflect the regions that are kinematically associated. Based on these findings, HNCO may prove to be a useful probe for disentangling kinematic structure in these sorts of regions, perhaps due to its unique formation pathway, as discussed in Section 4.3.4.

To compute the column densities of CH<sub>3</sub>OH, HCN, and HNCO, we utilize the non-LTE radiative transfer code, RADEX (Van der Tak et al. 2007). As inputs of the gas temperatures, we adopt the physical conditions determined in Paper I, using a RADEX analysis of  $\sim 30$  transitions of CH<sub>3</sub>OH observed with the CSO. As the CSO observations only included single pointings toward B1, encompassing B1a, B1b, and B0d, and toward B2, containing B2a, B2b, and B2d, we only computed the column densities in these six regions. While a similar analysis could be performed for the remainder of B0, previous estimates for the

kinetic temperatures and gas densities throughout B0 have not been consistent in the literature (Choi et al. 1999; Bachiller et al. 2001). It should be noted that further observations could help constrain the physical environment in B0, which would provide contrast to B1 and B2 shocks.

We apply derived parameters of  $T_k = 60$  K,  $n_{\text{H}_2} = 3 \times 10^5$  cm<sup>-3</sup> toward B1 and  $T_k = 50$  K,  $n_{\text{H}_2} = 6 \times 10^5$  cm<sup>-3</sup> toward B2. While Paper I used a Two-component fit with an extended, cool component and a compact, warm component, we only adopt the warm component parameters, as the warm component should dominate the emission originating from these small clumps. With these input conditions and line parameters from the Gaussian fits to the spectra, we obtain column densities reported in Table 3.

For the purposes of this analysis, the spectral lines without anomalous features, such as non-symmetric broadening, significant self-absorption, and line-blending, were used to constrain the abundances. The individual cases are discussed below. The derived column densities of each species are given in Table 3. Liberal uncertainties are assumed due to the small number of transitions observed, asymmetric line profiles, and the inherit uncertainties discussed in Paper I to be  $\sim 32\%$ .

We further convert from column densities to abundances with respect to hydrogen. Bachiller & Pérez Gutiérrez (1997) determined that  $N_{\text{H}_2} \sim 10^{21}$  cm<sup>-2</sup> in B1 and  $N_{\text{H}_2} \sim 5 \times 10^{20}$  cm<sup>-2</sup> in B2 using the optically thick <sup>12</sup>CO line emission and conversion by  $N_{\text{H}_2} \simeq 10^4 N_{\text{CO}}$ . However, using measurements on the optically thin isotopologues of CO, such as <sup>13</sup>CO, higher column densities are derived. Additionally, multiple authors have suggested that a higher conversion factor of  $N_{\text{H}_2} \simeq 3 \times 10^4 N_{\text{CO}}$  may be more appropriate (Lefloch et al. 2012; Bolatto et al. 2013). Given these ambiguities, we adopt  $N_{\text{H}_2} \sim 2 \times 10^{21}$  cm<sup>-2</sup> toward B1 and  $N_{\text{H}_2} \sim 10^{21}$  cm<sup>-2</sup> toward B2 based on  $N_{\text{CO}} \sim 9 \times 10^{16}$  cm<sup>-2</sup> in B1 (Lefloch et al. 2012) and  $N_{\text{CO}} \sim 5 \times 10^{16}$  cm<sup>-2</sup> in B2 (Bachiller & Pérez Gutiérrez 1997).

Furthermore, roughly half of the CO line flux toward B1 arises within a blueshifted wing component in the velocity range of  $-15$  to  $-4$  km s<sup>-1</sup>, previously designated the  $g_2$  component (Lefloch et al. 2012). This wing component is evident in HCN and HCO<sup>+</sup>, but is absent from the profiles of CH<sub>3</sub>OH and HNCO, as seen in Figures 3 and 4. Similar effects have been described by Tafalla et al. (2010), but with their designated f-wing to range over  $-7.5$  to  $-3.5$  km s<sup>-1</sup>, as determined by the transition from optically thin to thick through the <sup>13</sup>CO(2–1) to CO(2–1) ratio at each given velocity.

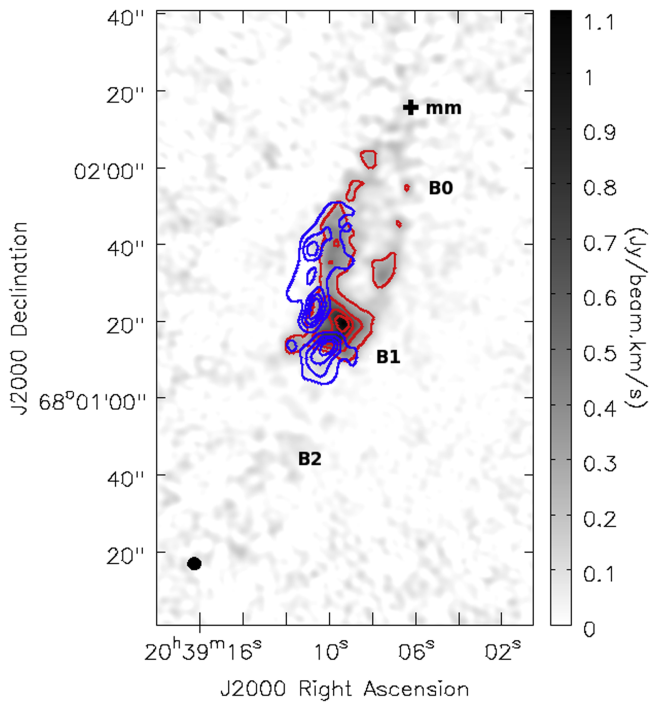


**Figure 4.** Integrated emission maps of the blue wing component of HCN (1–0) (blue contours at levels of 0.5, 1.0, 1.5, and 2.0 Jy beam<sup>-1</sup> km s<sup>-1</sup>) and HCO<sup>+</sup> (1–0) (raster, red contours at levels of 0.22, 0.45, 0.67, and 0.89 Jy beam<sup>-1</sup>). The velocity ranges of integration were both  $-15$  to  $+4$  km s<sup>-1</sup>. The synthesized beam size is displayed as filled black in the lower left.

Because CH<sub>3</sub>OH and HNCO do not exhibit this wing component, we focus on the primary velocity peak, which is more Gaussian shaped. Taking this feature into account, we estimate that  $N_{\text{H}_2} \sim 10^{21}$  cm<sup>-2</sup> in the primary component toward B1, in the  $g2$ -wing component of B1, and toward B2, in agreement with the derived hydrogen column within the slow wing of Tafalla et al. (2010). We assume that this hydrogen column density is the same toward all six clumps. As is typical of abundance measurements, the reported abundances are therefore approximate, and relative abundances determined from lines within this data set are more precise. Below, we briefly discuss the spectrum of each molecule and observed patterns in column density and abundance.

### 3.2.1. CH<sub>3</sub>OH

We detect the four  $2_k-1_k$  transitions of CH<sub>3</sub>OH in all of the clumps used in this study, and we detect weak CH<sub>3</sub>OH emission toward the stellar source, consistent with previous observations (Gómez-Ruiz et al. 2013). The relative intensities of the three stronger lines ( $2_{-12}-1_{-11}$ ,  $2_{02}-1_{01}++$ ,  $2_{02}-1_{01}$ ) remained a very consistent ratio of 4:3:1, respectively, throughout the regions. We note the presence of a small wing on the blueshifted side of the CH<sub>3</sub>OH line profiles toward B1a and b and toward B0a, c, d, and e. This wing component spans a velocity range of  $-4$  to  $-2$  km s<sup>-1</sup>, which is distinct from the  $g2$  wing component which extends to  $-15$  km s<sup>-1</sup>. This has been observed previously by Gómez-Ruiz et al. (2013). As was also reported by Gómez-Ruiz et al. (2013), CH<sub>3</sub>OH emission in L1157B is detected at velocities only slightly blueshifted ( $|\Delta v_{\text{LSR}}| < 3.5$  km s<sup>-1</sup>) to the cloud velocity, with generally larger offsets observed at distances further from L1157-mm

(Table 4). There is also a small, blue wing with a width of  $\sim 4$  km s<sup>-1</sup> observed toward B1 and B0a, c, d, and e. Since B1 is located at the apex of the bow shock, this wing may originate from the terminal velocity of the shock as it propagates into cold, dense, unshocked material.

The reported column density for CH<sub>3</sub>OH is the SNR-weighted average of the individual column densities derived per transition using RADEX. The column densities remained fairly consistent for the various regions, being on the order of  $\sim 1.5$ – $2.7 \times 10^{15}$  cm<sup>-2</sup>. Similarly, the abundances relative to hydrogen are estimated to be  $\sim 1.5$ – $2.7 \times 10^{-6}$ , with the highest abundances toward B2a. These are displayed in Table 3. These values are consistent with the results of Paper I, which obtained column densities of  $\sim 3 \times 10^{15}$  cm<sup>-2</sup> from CSO observations toward B1 and B2. The small differences in column densities may be attributed to Paper I’s use of a two-component fit in the RADEX analysis, as well as some of the extended emission from CH<sub>3</sub>OH in the cooler component being resolved out by CARMA’s beam. Given the general agreement with previous observations, we will study the abundance enhancement of other observed molecules relative to methanol.

### 3.2.2. HCN

HCN has been detected in all clumps studied in L1157B, as well as the stellar source. Velocity offsets of HCN (1–0) were observed to be slightly blueshifted to the systemic velocity, but with no significant gradient over distance from L1157-mm observed. As seen in Figure 3, the three hyperfine components are clearly resolved, and we report two anomalous features.

First, the  $F = 0-1$  hyperfine component is seen to be broadened and contains a prominent blueshifted wing toward most clumps in B0 and B1, as seen in previous observations of this line (Benedettini et al. 2007). This component is associated with the  $g2$  component observed in CO (Lefloch et al. 2012) as well as in HCO<sup>+</sup> in our observations. Here, the lower-frequency edge of the blue wing was set by where the morphology of the line emission significantly changed before the peak of the  $F = 0-1$  transition. The integrated HCN (1–0) emission in the velocity range of  $-15$  to  $-4$  km s<sup>-1</sup>, with respect to the  $F = 0-1$  hyperfine component, is shown in Figure 4 overlaid on HCO<sup>+</sup> emission within this velocity range. This velocity component clearly maps to the apex and eastern wall of C2 and is notably absent toward B2. This may imply that the wing emission originates from the shock as it propagates through the semi-processed material between C1 and C2, and thus has not been significantly slowed down. This is further evidenced by SiO emission, which displays broader velocity wings ( $\sim 20$  km s<sup>-1</sup>; Gómez-Ruiz et al. 2013). This will be further discussed later.

The second anomalous feature in the spectrum is a strong line at  $\sim 4$  km s<sup>-1</sup>, with respect to the  $F = 1-1$  transition, toward B2a, B2b, and B2d. This can be seen in B2a of HCN in Figure 3. The integrated emission of this fourth component can be seen in Figure 5 to be nearly exclusively in B2. The flux observed in B1a and the eastern wall of B0 is blended emission from the red tail of the  $F = 1-1$  line and not a separate component. This supposed fourth line could be explained by a second, prominent velocity component redshifted by approximately the hyperfine spacing. This would result in the central two observed features being a blend of two components,  $F = 2-1/F = 0-1$  and  $F = 1-1/F = 2-1$  for the second and third most blueshifted features, respectively. Meanwhile, the

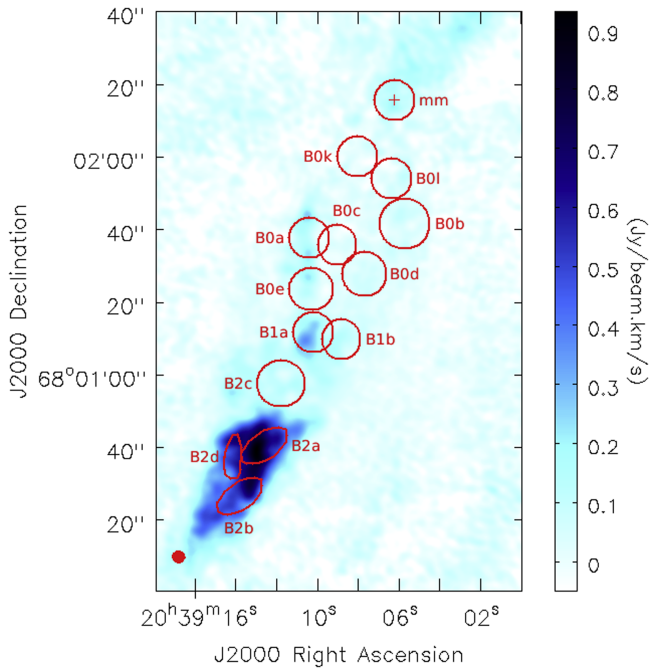


**Figure 5.** Integrated emission maps of the 4th unknown component near HCN (1–0), with the regions defined in Table 2 displayed in red, along with the stellar source. The synthesized beam size is displayed as filled red in the lower left.

outer two features are unblended, single-transition features  $F = 0-1$  and  $F = 1-1$  for the first and fourth most blueshifted features, respectively. However, the relative emission strengths of the hyperfine components do not clearly indicate this is the case. Further, it is curious that a redshifted component is not apparent in the spectral lines of other species observed in B2, and no similar feature has been reported in the literature for another molecule. But if the feature is a second velocity component, then this would provide further evidence that B2c is kinematically related to the apex of C2, and not to the rest of B2. Another possible explanation could be that this is an unidentified line of a separate species, which may explain why it is primarily in B2, similar to HNC. However, it seems unlikely that we would observe an unknown transition of similar strength to HCN (1–0), with no reasonable candidate transitions within the NRAO Splatalogue database.<sup>8</sup> Observation of the HCN (2–1) has the potential to clarify the scenario.

Finally, the observed line intensity ratios of HCN were distinct from the optically thin, LTE hyperfine line ratios of  $F = (2-1):(1-1):(0-1) = 5:3:1$ . The observed ratios are about  $\sim 1.76:1.35:1$ , respectively. While we do not expect LTE conditions, these line ratios cannot be accounted for by RADEX under physical conditions consistent with previous observations of L1157. This may indicate a pumping process producing weak masing, which should be accounted for by RADEX. It is also possible that, in part, the potential two blended velocity components discussed previously may cause some of the deviation from the thermal line ratios. Recent work by Mullins et al. (2016) on anomalous hyperfine line strengths also point to a strong dependency on optical depth in combination with gas infall or dynamics as a potential explanation of these observed ratios.

<sup>8</sup> Available at [www.splatalogue.net](http://www.splatalogue.net) (Remijan et al. 2007).

Because the blue wing component appears to be associated with different gas than the clumps, we report HCN column densities from RADEX calculations solely on the  $F = 1-1$  transition. This hyperfine line should not include substantial flux contributed by the blueshifted wing. It has been previously shown that accurate modeling of HCN hyperfine transitions requires that radiative transfer calculations be explicitly applied to each  $F$ -level independently. In particular, the  $J = 1-0$ ,  $F = 0-1$  transition is prone to producing spurious results, especially when the line ratios are not well-described by a single excitation temperature (Mullins et al. 2016). The derived column densities are of the order of  $10^{13}$ – $10^{14}$   $\text{cm}^{-2}$ , as shown in Table 3, with higher column densities toward B1a and B2. The HCN to  $\text{CH}_3\text{OH}$  column density ratio varied between  $1.7$ – $5.3 \times 10^{-2}$ . Benedettini et al. (2007) reported larger column densities by up to an order of magnitude in all regions except B0d. However, they derived their column densities assuming LTE, whereas we utilized the non-LTE code RADEX (Van der Tak et al. 2007). The non-LTE approach is likely more accurate, especially given the non-thermal hyperfine ratios.

Benedettini et al. (2007) report that HCN (1–0) undergoes strong self-absorption in observations toward L1157B, which would result in an underestimation of their reported column density. It is interesting to note that toward all regions in L1157B the troughs between the hyperfine features lie very close to what would result from HCN residing in ambient gas (i.e., shifted by the systemic velocity of  $\sim 2.7$   $\text{km s}^{-1}$ ). The red side of each of these features also appears to fall off with slopes that are not indicative of a typical Gaussian profile, suggesting the line may be significantly self-absorbed. A possible analogous absorption feature is also observed in the  $\text{HCO}^+$  (1–0) emission. It does not appear that  $\text{CH}_3\text{OH}$  or HNC have similar self-absorption features.

If the observed profiles for HCN are indeed due to self-absorption, the abundances derived here would be underestimated. As a result, the molecular enhancements would be even larger than those determined here. We do not have sufficient data to make a claim as to the likelihood that this is self-absorption, but we suggest this may be an intriguing avenue for follow-up study.

### 3.2.3. $\text{HCO}^+$

$\text{HCO}^+$  has been detected toward each region in L1157B and in the stellar source. As seen in Figure 3, the emission displays significant self-absorption toward all positions in the outflow at a velocity of  $3$ – $4$   $\text{km s}^{-1}$ . However, this self-absorption is not detected toward the stellar source. Due to the non-Gaussian line shapes and the self-absorption, we do not fit the spectra or determine  $\text{HCO}^+$  column densities here.

The blueshifted  $g_2$  wing of  $\text{HCO}^+$  (1–0) is observed, spanning a similar velocity range of HCN (1–0). As shown in Figure 4, both of these blueshifted components map to the apex and eastern wall of C2, implying that the source of these emission wings may originate from the same physical structure. Figure 6 shows blue wing ( $v_{\text{LSR}} = -15$  to  $-3.86$   $\text{km s}^{-1}$ ) and red wing ( $v_{\text{LSR}} = 4.3$ – $10$   $\text{km s}^{-1}$ ) of the  $\text{HCO}^+$  emission along with the central peak ( $v_{\text{LSR}} = -3$  to  $3.5$   $\text{km s}^{-1}$ ). The transition from the blue wing to the central peak was determined by where the morphology significantly changed, as discussed above, while the red wing/central peak boundary was the velocity where the self-absorption was strong enough to make



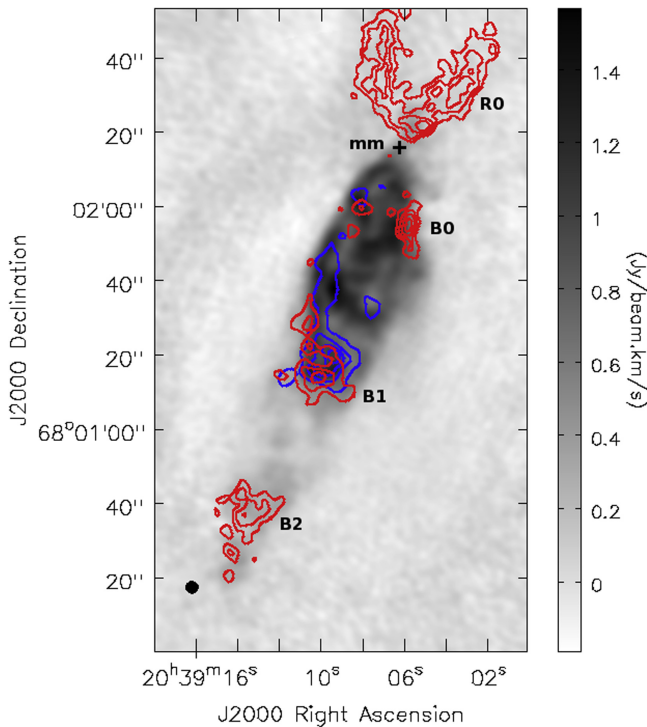


**Figure 6.** Integrated emission map of  $\text{HCO}^+$  (1–0) with contours of its blue wing ( $-15$  to  $-3.86$   $\text{km s}^{-1}$  at levels of 0.18, 0.37, 0.55, and  $0.74$   $\text{Jy beam}^{-1}$ ) and red wings ( $+4.3$  to  $+10$   $\text{km s}^{-1}$  at levels of 0.08, 0.16, 0.24, and  $0.33$   $\text{Jy beam}^{-1}$ ) in their respective colors over the central peak raster ( $-3$  to  $+3.5$   $\text{km s}^{-1}$ ). The synthesized beam size is displayed as filled black in the lower left.

the observed line strength effectively zero. Here, the central peak is observed to trace the ambient gas throughout the C1 cavity, with a slight peak along the ridge. The redshifted emission continues far past the stellar source, as would be expected. Interestingly, there are also redshifted components also observed at concentrated peaks along the apex of B0/1, B0 $\ell$ , and B2. While these are not necessarily separate components, it is possible that the emission originates from gas from the far side of the C1 and C2 cavity.

### 3.2.4. HNCO

HNCO was detected toward all of the regions in L1157B, but not toward the stellar source. Although weak, a wing component from  $-3$  to  $-1$   $\text{km s}^{-1}$  is apparent in the spectra toward B1 and the ridge of B0. This occupies the same velocity range and general spatial distribution as the weak wing component in  $\text{CH}_3\text{OH}$ , but is distinct from the  $g2$  component evident in the spectra of HCN and  $\text{HCO}^+$ . Our RADEX calculations based on our Gaussian fits determine the column densities of HNCO to vary between  $\sim 2.5$ – $8.0 \times 10^{13}$   $\text{cm}^{-2}$  across the entire line, comparable to the measured column densities of HCN. A factor of 2 increase in column density between B2 and B1 is immediately apparent. This corresponds to the  $N(\text{HNCO})/N(\text{CH}_3\text{OH})$  increasing by a factor of 2 ( $\sim 1.7 \times 10^{-2}$  to  $\sim 3.5 \times 10^{-2}$ ) and similar for abundance enhancement relative to  $\text{H}_2$ , which is consistent with previous observations (Mendoza et al. 2014).

### 3.2.5. $\text{CH}_3\text{CN}$

A significant feature appears in three edge channels of one of our windows. Given a similar velocity profile as our other observed molecules, the transition appears to coincide with the

$5_k-4_k$  transition of  $\text{CH}_3\text{CN}$ . The integrated emission of these three channels display a distribution similar to  $\text{CH}_3\text{OH}$ , with significant emission observed throughout the major shocked regions of L1157B. Very little emission appears to come from any of the less prominent shocks and ambient gas. It has been detected previously in B1 in  $14_k-13_k$  (Arce et al. 2008) and mapped in  $8_k-7_k$  (Codella et al. 2009), with a distribution consistent with our observations. These both report column densities between  $10^{12}$  and  $10^{13}$   $\text{cm}^{-2}$ .

## 4. DISCUSSION

A few trends emerge from the results. First, it is apparent that the northernmost clumps in B0 are kinematically distinct from the material in the south of the ridge. Further, the clumps in B1 and south of the ridge in B0 are more kinematically and structurally similar compared to northern B0. Second, a broad ( $\sim 15$   $\text{km s}^{-1}$ ) component, referred to as  $g2$ , has been observed in HCN and  $\text{HCO}^+$ , as well as CO and SiO in previous work (Lefloch et al. 2012). It is predominately located along the eastern wall of the C2 cavity and near the apex of C2, most significantly toward B0e. This component contributes a significant fraction of the molecular line emission by these species in the eastern portion of C2. Furthermore, we notice possible east–west differentiation within C2 and also between B1 and B2.

### 4.1. East/West Chemical Contrast in C2

Previous literature has discussed the existence of a chemical differentiation within C2 (Tafalla & Bachiller 1995; Gueth et al. 1998; Bachiller et al. 2001; Benedettini et al. 2007, 2013). While species including HCN and SiO produce strong line emission along the eastern wall of C2, other molecules such as  $\text{CH}_3\text{OH}$  and OCS are seen stronger along the western wall, especially toward the apex. We observe this trend in the species studied here as well. In our CARMA images,  $\text{CH}_3\text{OH}$  is seen to be strongest at the western wall of B1 and along the ridge in B0, although this relative abundance enhancement is less significant compared to the other studied species. With the first interferometric maps of HNCO presented here, it can be seen that this species is even more concentrated to the eastern wall of C2 than  $\text{CH}_3\text{OH}$ . Meanwhile, HCN is substantially stronger on the eastern wall compared to the western. As the  $g2$  component preferentially contributes to the emission seen in the eastern wall, it is plausible that the apparent differentiation results from the contribution of this wing. However, considering only the emission by the HCN (1–0)  $F = 1-1$  transition, for which the wing component should not contribute substantially, it appears that the east–west differentiation still persists. As reported previously, the column density of  $\text{CH}_3\text{OH}$  is relatively consistent near the apex of C2, while a significant enhancement is observed for HCN in B1a over B1b (Benedettini et al. 2013). In our analysis, we found this to be an increase of column density of about a factor of two, which is a similar enhancement found along the eastern wall up to the ridge.

Bachiller et al. (2001) assert such chemical segregation is due to chemical stratification within the cloud. Gueth et al. (1996) proposed that as the precessing jet sweeps from east to west, the western wall of C2 would be interacting with new, unshocked material in the molecular cloud. Meanwhile, the

eastern wall is expanding into material already processed during the previous shock that produced C1.

In the western wall, especially toward the apex in B1, abundances would be indicative of prototypical ice mantle desorption as the shock interacts with grains that previously resided in cool, quiescent gas. This results in an enhancement of grain-species, which we observe with CH<sub>3</sub>OH and HNCO. On the other hand, the eastern wall is interacting with dust grains that have already been recently shocked by the B2 event. As a result, the ice mantles would not have had time to redeposit onto the surface of the grains. The shock would instead destroy the complex species that were brought into the gas phase during the first shock, and further erode the bare dust grain. The resulting products of these complex molecules would then be enhanced in these regions, as seen in HCN and HCO<sup>+</sup>. This is supported by the reported anti-correlation of CN and HNCO in this region (Rodríguez-Fernández et al. 2010), as CN is likely to be the product of this destruction. In addition, this also explains the distribution of SiO toward the eastern wall of C2, as it would be enhanced in the shocking of bare-grains compared to grains with significant ice-mantles. In Benedettini et al. (2007), emission from HC<sub>3</sub>N, HCN, CS, NH<sub>3</sub>, and SiO were found to be brighter in eastern clumps in C2, while CH<sub>3</sub>OH, OCS, and <sup>34</sup>SO emissions were more prominent in western clumps. The segregation of these specific species aligns with our proposed scenario.

This scenario is further supported by the velocity wings observed in these species. While the chemical differentiation within C2 is seen both in the wing and the primary velocity components, the wing components probe the properties of the shock that would affect the chemistry in the entire region. CH<sub>3</sub>OH and HNCO are observed to have a small, ~4 km s<sup>-1</sup> blue wing primarily toward B1b, as was previously discussed. This wing could be tracing the shock as it hits, and is thus slowed down, by the cold, dense, and unshocked gas. Meanwhile, HCO<sup>+</sup> and HCN are observed to have a large, blue, g2 wing primarily toward B1a and the eastern wall of C2. Here, the shock would not be slowed down because it is interacting with gas that has already been processed and recently shocked, and thus is less dense than toward B1b. This higher-velocity scenario is also supported by the higher abundance of SiO toward the eastern wall, as it is produced more efficiently in high-velocity shocks, and where the dust grains are already bare due to the previous shock.

It should be noted that observations by Gómez-Ruiz et al. (2013) of a pair of H<sub>2</sub>CO lines with differences of excitation energies of  $\Delta T \sim 47$  K show significantly different emission on opposite edges of B1, suggesting these asymmetries could instead be due to excitation effects. However, the majority of the lines studied here have relatively low excitations and still display chemical differentiation. A follow up study of higher energy transitions of these species would help determine the significance of excitation on the chemical differentiation in C2. Recent observations of isotopologues of CO by Kwon et al. (2015) may suggest that there are in fact two bipolar jets, each of which could contribute to a different wall of C2. While this may explain the asymmetric brightness of certain lines, this does not necessarily explain the distinct chemical segregation within the region.

## 4.2. Enhancements in B2

Among the species studied, abundances toward the shocked regions in B2 were found to be either equivalent or higher compared to the B1 shocks. The abundance relative to H<sub>2</sub> of HCN toward B2a and B1a are nearly equivalent. For CH<sub>3</sub>OH, B2 appears to be enhanced, although it is only just outside of our reported uncertainties. Also, in HNCO, we see a factor of two increase in abundance relative to CH<sub>3</sub>OH. Meanwhile, HCO<sup>+</sup> emission is significantly weaker in B2 relative to B0 and B1. To determine what may cause this difference, it is necessary to determine how B1 and B2 vary.

Since the shock in B2 is older than in B1, the observed abundances could be a result of viewing changes on a chemically relevant timescale. If this proves significant, then it would imply that the initial liberation of molecules from the grain by the shock may not be the only prominent process that occurs in these environments. Instead, post-shock, gas-phase reactions would become significant, as these regions are at higher densities and temperatures than the pre-shock environments. Examples of these will be discussed briefly in Section 4.3.

Gómez-Ruiz et al. (2013) have also proposed that the shock in B2 is ~10 km s<sup>-1</sup> faster than B1 from observations of SiO and its line profile. Higher shock velocities can result in more efficient erosion of ices on grain surfaces and the mantles themselves, as has been shown in models of sputtering on grains. (Jiménez-Serra et al. 2008; Van Loo et al. 2013). If this difference in shock velocities is significant to the proceeding chemistry, then the higher abundances of CH<sub>3</sub>OH and HNCO could be explained by a higher liberation rate from the grain.

## 4.3. Formation Chemistry Implications

### 4.3.1. CH<sub>3</sub>OH

Overall, the consistent abundance of CH<sub>3</sub>OH indicates that its primary source is from the liberation of grains during the shock. The slightly higher abundances toward the relatively cooler, older shock, B2, may imply that the CH<sub>3</sub>OH may have a production pathway as the young shock-tracing molecules react following their initial release into the gas phase. Chemical models of outflows have shown that methanol abundance is elevated in higher gas density regions, from 10<sup>5</sup> to 10<sup>6</sup> cm<sup>-3</sup> (Viti et al. 2004). This difference in density was observed when comparing the gas densities of B1 and B2 from Paper I, supporting this interpretation. Rawlings et al. (2013) has discussed that recently shocked material surrounding the grains is at high enough densities that three-body reactions may occur efficiently, such as with CH<sub>3</sub>, OH, and H<sub>2</sub>O (as a passive third body) to produce CH<sub>3</sub>OH. It is also possible that the larger shock velocity in B2 relative to B1, as proposed by Gómez-Ruiz et al. (2013), could result in a more efficient liberation of grain species.

### 4.3.2. HCN

If the scenario proposed for the east/west chemical differentiation is valid, then the formation of HCN would be significantly impacted by the formation of CN from the destruction of more complex species in the gas phase. Following the enhancement of CN in the region, HCN could be readily produced as well. Similar iterations of this interpretation have been proposed by Benedettini et al. (2007).

### 4.3.3. $\text{HCO}^+$

The strong emission of  $\text{HCO}^+$  toward the region not directly associated with the shock front, B0, is consistent with previous work, where the molecule is thought to be rapidly produced in the gas phase. Rawlings et al. (2004) found that  $\text{HCO}^+$  is enhanced in the boundary layer between the jet and the surrounding ambient gas, which is observed here. Within this region, the shock will cause  $\text{H}_2\text{O}$  and  $\text{CH}_3\text{OH}$  to be lifted from the grains. With these species abundant in the gas phase, sufficient amounts of the ions  $\text{H}_3\text{O}^+$  and  $\text{CH}_3\text{OH}_2^+$  can be formed to rapidly produce  $\text{HCO}^+$ . Once  $\text{HCO}^+$  resides in this high-temperature, water-rich environment, it may then be efficiently destroyed through dissociative recombination (Bachiller et al. 2001) or through a reaction with  $\text{H}_2\text{O}$  (Bergin et al. 1998). Bergin et al. (1998) found that  $\text{HCO}^+$  could be efficiently converted into  $\text{H}_3\text{O}^+$  and CO on the order of 100 years, or the approximate timescale of the shock passage modeled. This points to the eastern wall of C2 being the site of a recent interaction, as observed by the wing feature of HCN and  $\text{HCO}^+$  seen toward this region. Then, as the shock evolves, the  $\text{HCO}^+$  is rapidly destroyed, as evidenced by the weaker emission toward B1 and B2.

### 4.3.4. $\text{HNCO}$

$\text{HNCO}$  has been studied in gas-grain warm-up chemical models of hot corinos, and was found to be formed through the gas-phase destruction of more complex molecules after they are lifted from the grain surface (Garrod et al. 2008; Quan et al. 2010). In the high temperature phase of the hot core models, the gas-phase abundances were found to be only  $2 \times 10^{-9}$ . However in some models, the peak abundance on the grain prior to desorption due to the warm up, was as high as  $\sim 10^{-8}$ – $10^{-7}$ .

Hypothetically, this would imply that, in a hot-core-like environment, the observed abundances could be explained by all of the  $\text{HNCO}$  on the grain suddenly being lifted from the grain. However, Rodríguez-Fernández et al. (2010) argue that the gas-phase chemistry within shocks should differ due its higher temperatures and densities over a short period of time. They propose the dominant pathways to be (a) the initial grain erosion increasing the  $\text{HNCO}$  then (b) neutral-neutral gas phase reaction of CN and  $\text{O}_2$  to produce OCN, which may be favored due to the significant enhancement of  $\text{O}_2$  within the post-shock gas (Bergin et al. 1998; Gusdorf et al. 2008). The OCN can then be rapidly converted into  $\text{HNCO}$ .

This formation pathway is consistent with the fact that  $\text{HNCO}$  is currently the only non-sulfur-bearing molecule observed to have significantly greater enhancement in B2 than B1. This is because the efficient formation of both  $\text{HNCO}$  and several sulfur-bearing species (i.e., SO and  $\text{SO}_2$ ) heavily relies on molecules reacting with the abundant species  $\text{O}_2$ , converting CN to  $\text{HNCO}$ , and  $\text{H}_2\text{S}$  to SO and  $\text{SO}_2$ . CN and  $\text{HNCO}$  have anticorrelated physical distributions, supporting this pathway (Rodríguez-Fernández et al. 2010). Further observations of other species associated with the  $\text{O}_2$  chemistry in shocks may help constrain the significance of this pathway. Again, the cause of this enhancement may also be due to B2's high shock velocity compared to B1.

## 5. CONCLUSIONS

We report high-resolution interferometric maps of emission from  $\text{CH}_3\text{OH}$ , HCN,  $\text{HCO}^+$ , and  $\text{HNCO}$  toward the southern outflow of L1157 from CARMA observations. In addition to defining three new clumps (B0k, B0l, and B2d), we utilized the non-LTE code RADEX to constrain the column densities and abundances of three of our species. We find the following.

1. The abundance of  $\text{CH}_3\text{OH}$  is relatively consistent across the regions and appears to be primarily produced by the liberation off of grain surfaces due to shocks.
2. Both HCN/ $\text{HCO}^+$  and  $\text{CH}_3\text{OH}/\text{HNCO}$  display velocity profiles that are indicative of their originating from the same physical regions.
3. The east/west chemical differentiation observed in B0 and B1 could be explained by the difference in shock-chemistry that occurs when the impacted medium is cold, dense, and quiescent or warm, diffuse, and previously shocked, as evidenced by the molecular enhancement and velocity profiles.
4. Through the first interferometric maps of  $\text{HNCO}$ , enhanced abundances are seen toward B2 relative to B1, which may be explained by the importance of the formation of  $\text{O}_2$  in shocked regions or by differences in shock velocities.

E.H., A.M.B, and C.N.S. thank the National Science Foundation (NSF) for continuing to support the astrochemistry program at the University of Virginia and the NASA Exobiology and Evolutionary Biology Program through a subcontract from Rensselaer Polytechnic Institute. N.M.D. gratefully acknowledges funding by the National Radio Astronomy Observatory Summer Research Internship, a Research Experience for Undergraduates funded by the NSF and Peter Teuben for helpful discussion. B.A.M. gratefully acknowledges funding by an NSF Graduate Research Fellowship during initial portions of this work. The National Radio Astronomy Observatory is a facility of the National Science Foundation operated under cooperative agreement by Associated Universities, Inc. Portions of this material are based upon work at the Caltech Submillimeter Observatory, which was operated by the California Institute of Technology under cooperative agreement with the National Science Foundation (AST-0838261). Support for CARMA construction was derived from the Gordon and Betty Moore Foundation, the Kenneth T. and Eileen L. Norris Foundation, the James S. McDonnell Foundation, the Associates of the California Institute of Technology, the University of Chicago, the states of California, Illinois, and Maryland, and the National Science Foundation. CARMA development and operations were supported by the National Science Foundation under a cooperative agreement, and by the CARMA partner universities.

## APPENDIX A

### SPECTRA FOR ALL MOLECULES AND REGIONS

For each of the species observed with CARMA (see Table 1), the spectra for all of the defined regions in Table 2 are provided below in Figures 7–10. For species with multiple transitions,  $\text{CH}_3\text{OH}$  and HCN, the velocities displayed are relative to the rest frequency of the central transition. For HCN, the unknown feature discussed in Section 3.2.2 is marked with a blue dashed line.

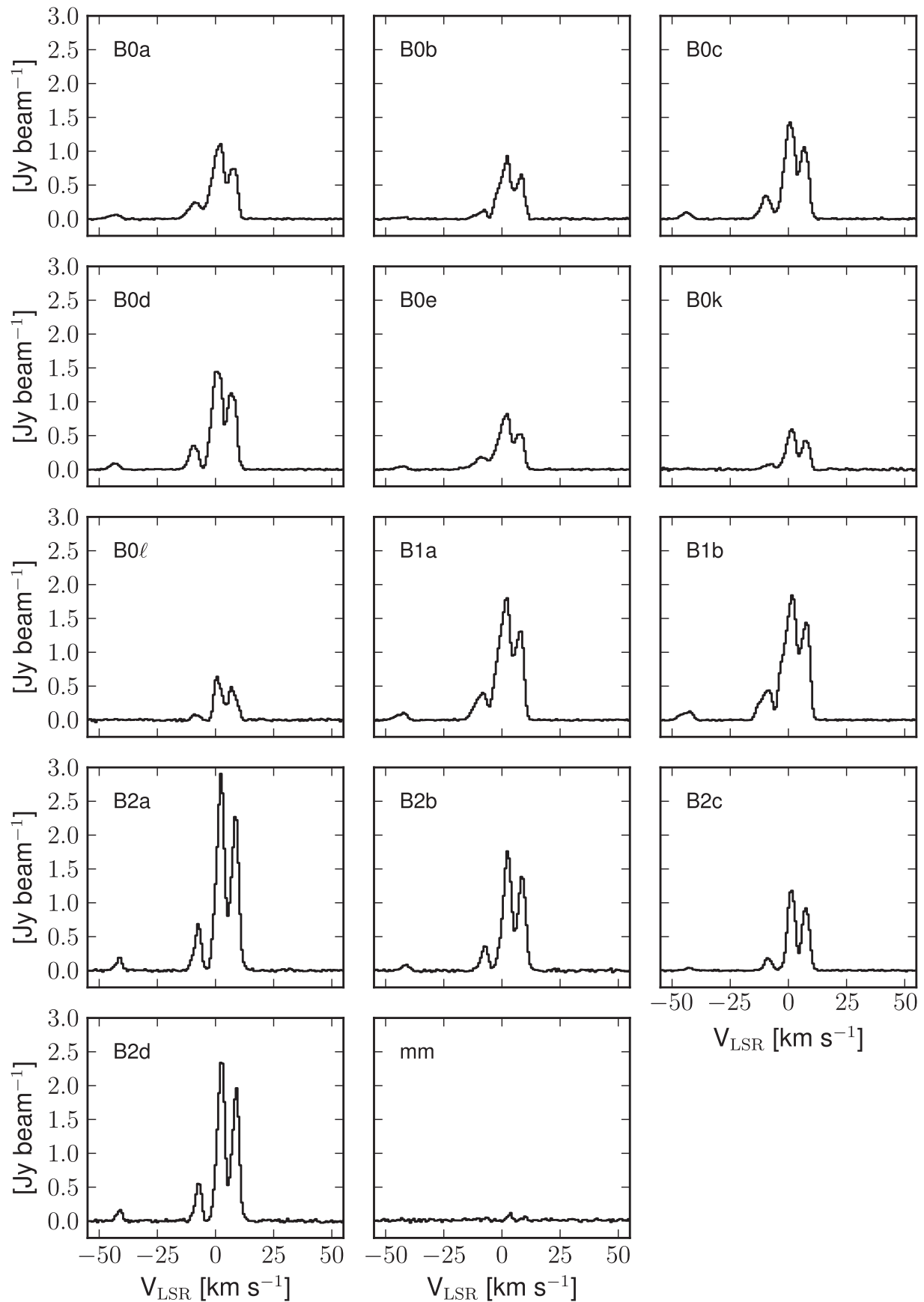
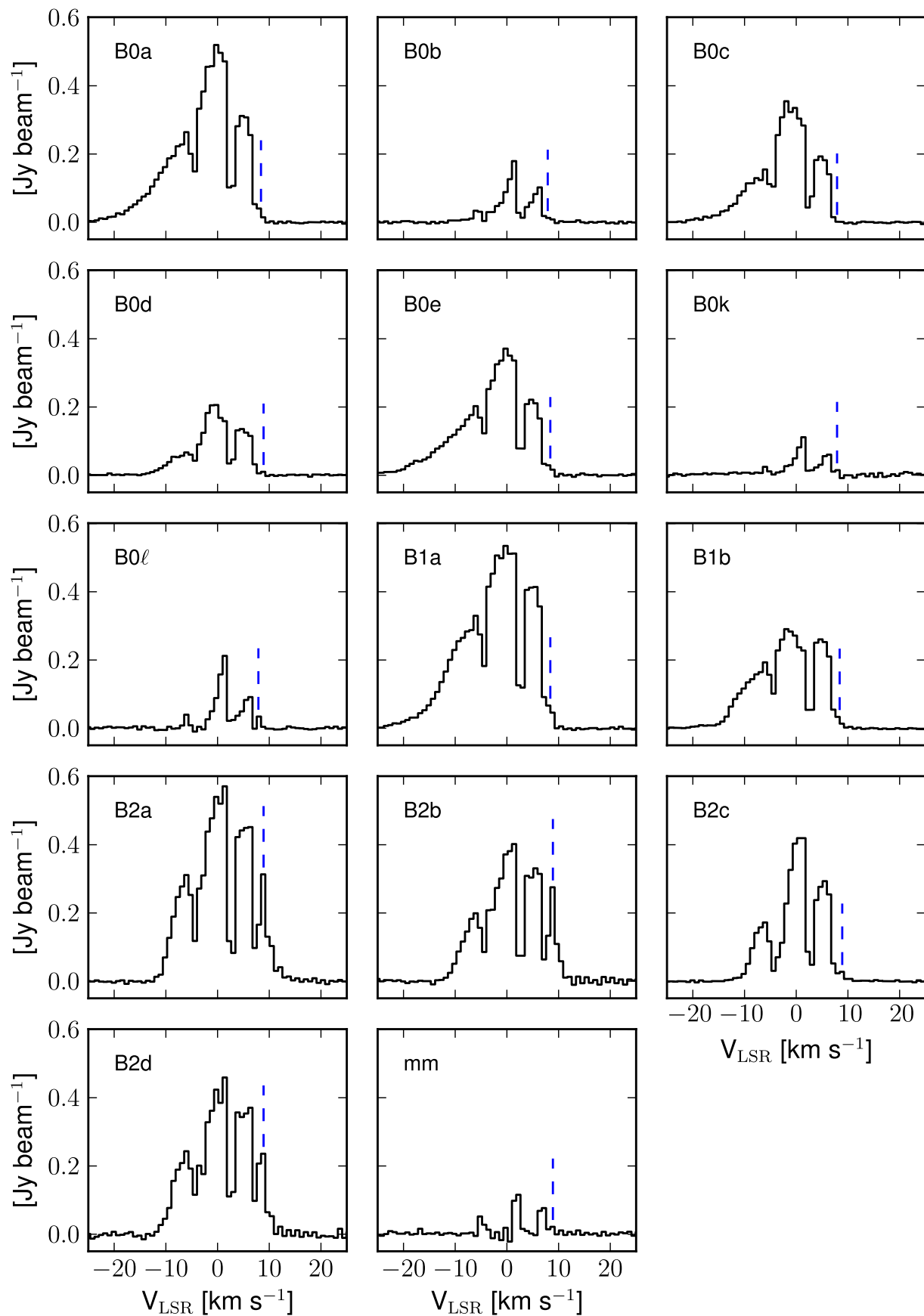
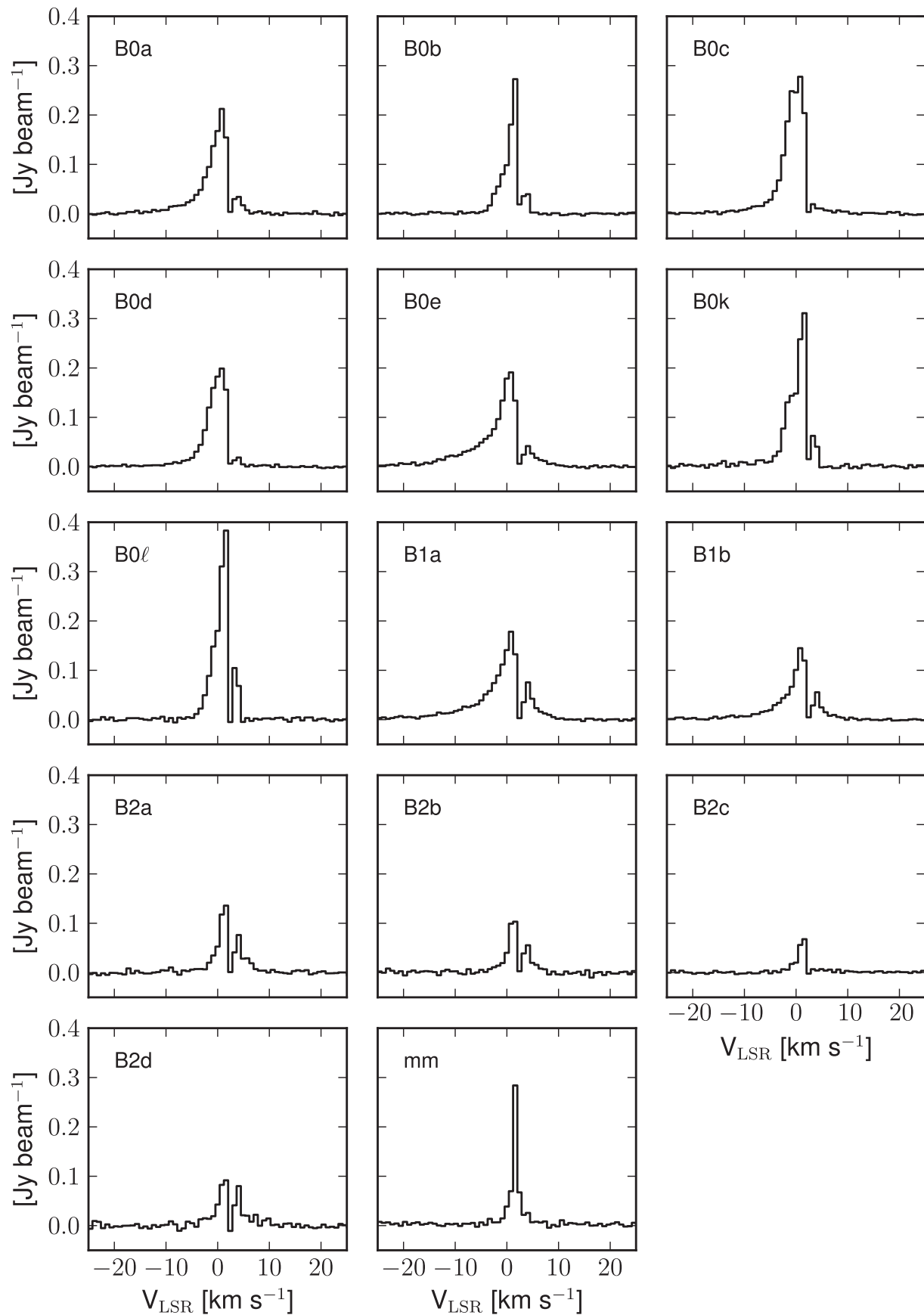


Figure 7. Extracted spectra of all regions in Table 2 for  $\text{CH}_3\text{OH}$  emission from the CARMA observations.



**Figure 8.** Extracted spectra of all regions in Table 2 for HCN emission from the CARMA observations. The unknown feature is marked with a blue dashed line.



**Figure 9.** Extracted spectra of all regions in Table 2 for  $\text{HCO}^+$  emission from the CARMA observations.

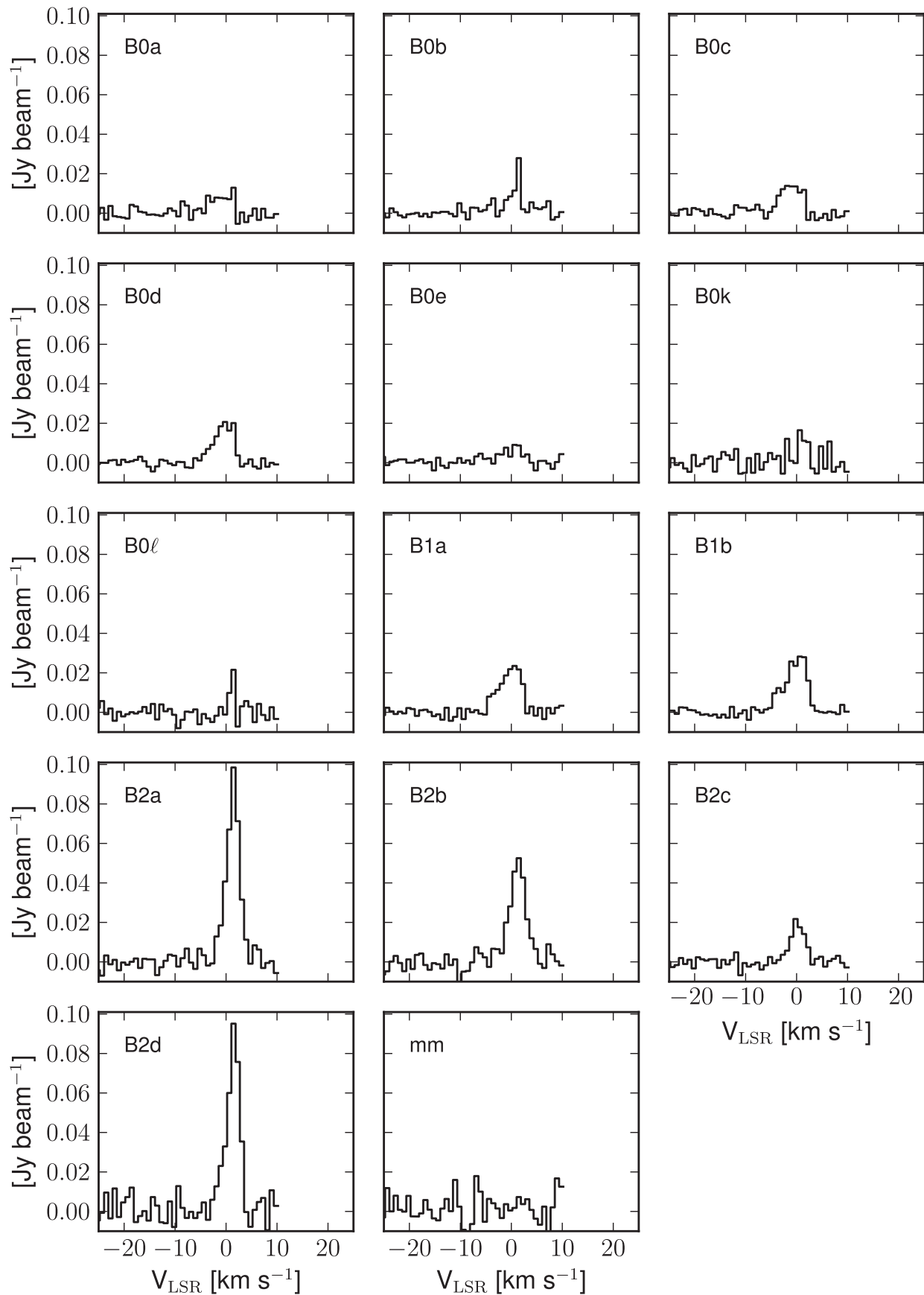


**Figure 10.** Extracted spectra of all regions in Table 2 for HNC O emission from the CARMA observations.

APPENDIX B  
TABLES OF SPECTRAL FITS FOR ALL MOLECULES  
AND REGIONS

For each of the species observed with CARMA (see Table 1), the parameters of the Gaussian fits of the spectra are tabulated below in Tables 4–6 for all of the defined regions in Table 2. Gaussian profiles were generated utilizing a modified version of the line fitting code described in Corby et al. (2015). The fourth column in Tables 4 and 5 and third column in Table 6 shows the LSR velocity of the line peak. For HCN, the unknown feature seen in B2 is listed as the “4th component.”

Table 4  
CH<sub>3</sub>OH Spectral Fits

Region	Transition	Peak (K)	$v_{\text{LSR}}$ (km s <sup>-1</sup> )	Line Width (km s <sup>-1</sup> )
B0a	2 <sub>-1,2</sub> -1 <sub>-1,1</sub>	2.92	1.30	3.63
	2 <sub>0,2</sub> -1 <sub>0,1</sub> ++	4.25	1.02	6.26
	2 <sub>0,2</sub> -1 <sub>0,1</sub>	0.91	0.81	7.03
B0b	2 <sub>1,1</sub> -1 <sub>1,0</sub>	0.24	0.00	5.48
	2 <sub>-1,2</sub> -1 <sub>-1,1</sub>	2.37	1.70	3.32
	2 <sub>0,2</sub> -1 <sub>0,1</sub> ++	3.20	1.30	6.82
B0c	2 <sub>0,2</sub> -1 <sub>0,1</sub>	0.42	0.59	5.05
	2 <sub>1,1</sub> -1 <sub>1,0</sub>	0.08	0.28	5.86
	2 <sub>-1,2</sub> -1 <sub>-1,1</sub>	4.13	0.46	3.94
B0d	2 <sub>0,2</sub> -1 <sub>0,1</sub> ++	5.60	0.28	5.58
	2 <sub>0,2</sub> -1 <sub>0,1</sub>	1.31	-0.15	5.14
	2 <sub>1,1</sub> -1 <sub>1,0</sub>	0.38	-0.46	4.59
B0e	2 <sub>-1,2</sub> -1 <sub>-1,1</sub>	4.58	0.62	4.12
	2 <sub>0,2</sub> -1 <sub>0,1</sub> ++	5.93	0.40	5.33
	2 <sub>0,2</sub> -1 <sub>0,1</sub>	1.44	0.06	4.25
B0k	2 <sub>1,1</sub> -1 <sub>1,0</sub>	0.36	0.06	4.37
	2 <sub>-1,2</sub> -1 <sub>-1,1</sub>	2.03	1.36	3.59
	2 <sub>0,2</sub> -1 <sub>0,1</sub> ++	3.08	1.21	6.23
B0l	2 <sub>0,2</sub> -1 <sub>0,1</sub>	0.66	1.46	9.48
	2 <sub>1,1</sub> -1 <sub>1,0</sub>	0.18	0.34	4.65
	2 <sub>-1,2</sub> -1 <sub>-1,1</sub>	1.76	0.96	3.59
B1a	2 <sub>0,2</sub> -1 <sub>0,1</sub> ++	2.32	0.87	4.77
	2 <sub>0,2</sub> -1 <sub>0,1</sub>	0.27	1.58	6.69
	2 <sub>1,1</sub> -1 <sub>1,0</sub>	0.05	0.19	3.81
B1b	2 <sub>-1,2</sub> -1 <sub>-1,1</sub>	1.77	0.53	4.80
	2 <sub>0,2</sub> -1 <sub>0,1</sub> ++	2.51	0.56	3.59
	2 <sub>0,2</sub> -1 <sub>0,1</sub>	0.31	0.96	3.66
B1c	2 <sub>1,1</sub> -1 <sub>1,0</sub>	...	...	...
	2 <sub>-1,2</sub> -1 <sub>-1,1</sub>	4.78	1.39	3.38
	2 <sub>0,2</sub> -1 <sub>0,1</sub> ++	6.68	1.05	7.00
B1d	2 <sub>0,2</sub> -1 <sub>0,1</sub>	1.45	0.40	6.35
	2 <sub>1,1</sub> -1 <sub>1,0</sub>	0.38	0.31	5.36
	2 <sub>-1,2</sub> -1 <sub>-1,1</sub>	5.16	1.24	3.41
B1e	2 <sub>0,2</sub> -1 <sub>0,1</sub> ++	6.79	0.81	7.44
	2 <sub>0,2</sub> -1 <sub>0,1</sub>	1.63	-0.34	6.10
	2 <sub>1,1</sub> -1 <sub>1,0</sub>	0.47	-0.28	5.98
B1f	2 <sub>-1,2</sub> -1 <sub>-1,1</sub>	9.04	1.86	3.53
	2 <sub>0,2</sub> -1 <sub>0,1</sub> ++	10.80	1.83	4.18
	2 <sub>0,2</sub> -1 <sub>0,1</sub>	2.57	1.89	3.41
B1g	2 <sub>1,1</sub> -1 <sub>1,0</sub>	0.72	1.98	3.04
	2 <sub>-1,2</sub> -1 <sub>-1,1</sub>	5.56	2.01	3.63
	2 <sub>0,2</sub> -1 <sub>0,1</sub> ++	6.66	1.98	4.49
B1h	2 <sub>0,2</sub> -1 <sub>0,1</sub>	1.38	2.05	3.66
	2 <sub>1,1</sub> -1 <sub>1,0</sub>	0.32	1.98	3.66
	2 <sub>-1,2</sub> -1 <sub>-1,1</sub>	3.76	0.87	3.63
B1i	2 <sub>0,2</sub> -1 <sub>0,1</sub> ++	4.79	0.87	3.78
	2 <sub>0,2</sub> -1 <sub>0,1</sub>	0.71	0.74	3.75
	2 <sub>1,1</sub> -1 <sub>1,0</sub>	0.15	0.74	3.59

Table 4  
(Continued)

Region	Transition	Peak (K)	$v_{\text{LSR}}$ (km s <sup>-1</sup> )	Line Width (km s <sup>-1</sup> )
B2d	2 <sub>-1,2</sub> -1 <sub>-1,1</sub>	7.67	2.11	3.38
	2 <sub>0,2</sub> -1 <sub>0,1</sub> ++	9.21	2.08	3.87
	2 <sub>0,2</sub> -1 <sub>0,1</sub>	2.24	2.14	3.04
mm	2 <sub>1,1</sub> -1 <sub>1,0</sub>	0.63	2.14	2.91
	2 <sub>-1,2</sub> -1 <sub>-1,1</sub>	0.22	3.10	2.88
	2 <sub>0,2</sub> -1 <sub>0,1</sub> ++	0.41	3.01	2.51
	2 <sub>0,2</sub> -1 <sub>0,1</sub>	...	...	...
	2 <sub>1,1</sub> -1 <sub>1,0</sub>	...	...	...

Table 5  
HCN Spectral Fits

Region	Transition	Peak (K)	$v_{\text{LSR}}$ (km s <sup>-1</sup> )	Line Width (km s <sup>-1</sup> )
B0a	$J = 1-0, F = 1-1$	4.19	0.81	3.50
	$J = 1-0, F = 2-1$	6.11	0.10	5.90
	$J = 1-0, F = 0-1$	3.05	0.85	8.00
B0b	$J = 1-0, F = 1-1$	1.30	1.29	2.10
	$J = 1-0, F = 2-1$	2.74	1.12	2.30
	$J = 1-0, F = 0-1$	0.54	4.90	2.80
B0c	$J = 1-0, F = 1-1$	2.42	0.68	3.50
	$J = 1-0, F = 2-1$	4.34	-0.47	5.70
	$J = 1-0, F = 0-1$	1.69	-0.27	7.50
B0d	$J = 1-0, F = 1-1$	1.74	0.71	3.70
	$J = 1-0, F = 2-1$	2.36	-0.20	5.50
	$J = 1-0, F = 0-1$	0.79	0.54	5.60
B0e	$J = 1-0, F = 1-1$	2.79	0.74	3.70
	$J = 1-0, F = 2-1$	4.04	0.17	6.50
	$J = 1-0, F = 0-1$	2.49	2.16	8.00
B0k	$J = 1-0, F = 1-1$	0.98	1.32	2.20
	$J = 1-0, F = 2-1$	1.62	1.25	2.20
	$J = 1-0, F = 0-1$	0.38	1.52	1.20
B0l	$J = 1-0, F = 1-1$	1.64	1.22	2.10
	$J = 1-0, F = 2-1$	2.79	1.32	2.10
	$J = 1-0, F = 0-1$	0.46	1.45	1.30
B1a	$J = 1-0, F = 1-1$	6.02	0.81	3.40
	$J = 1-0, F = 2-1$	6.56	0.03	6.10
	$J = 1-0, F = 0-1$	3.14	0.41	7.80
B1b	$J = 1-0, F = 1-1$	3.56	0.71	3.40
	$J = 1-0, F = 2-1$	3.54	-0.41	5.90
	$J = 1-0, F = 0-1$	1.97	0.07	7.50
B2a	4th Component	5.25	4.50	1.60
	$J = 1-0, F = 1-1$	5.95	0.88	3.50
	$J = 1-0, F = 2-1$	6.32	0.17	5.70
B2b	$J = 1-0, F = 0-1$	3.42	0.88	4.70
	4th Component	3.57	4.43	1.80
	$J = 1-0, F = 1-1$	4.27	0.85	3.50
B2c	$J = 1-0, F = 2-1$	4.49	0.54	5.50
	$J = 1-0, F = 0-1$	2.08	1.89	5.00
	$J = 1-0, F = 1-1$	3.94	0.85	3.30
B2d	$J = 1-0, F = 2-1$	5.61	0.47	4.00
	$J = 1-0, F = 0-1$	2.08	0.71	3.90
	4th Component	3.53	4.23	1.70
mm	$J = 1-0, F = 1-1$	4.76	0.88	3.70
	$J = 1-0, F = 2-1$	5.48	0.30	5.00
	$J = 1-0, F = 0-1$	2.73	1.01	4.50
mm	$J = 1-0, F = 1-1$	1.17	2.44	1.52
	$J = 1-0, F = 2-1$	1.79	2.33	1.35
	$J = 1-0, F = 0-1$	0.72	2.54	1.25



**Table 6**  
HNC0 Spectral Fits

Region	Peak (K)	$v_{\text{LSR}}$ ( $\text{km s}^{-1}$ )	Line Width ( $\text{km s}^{-1}$ )
B0a	0.13	-0.68	4.88
B0b	0.38	1.74	1.30
B0c	0.21	-0.75	4.47
B0d	0.29	0.03	4.30
B0e	0.10	0.58	4.91
B0k	0.22	1.60	1.94
B0l	0.36	1.60	0.89
B1a	0.32	0.27	4.91
B1b	0.38	0.38	4.94
B2a	1.26	1.81	2.93
B2b	0.70	1.70	3.65
B2c	0.28	0.61	3.17
B2d	1.26	1.91	2.76
mm	...	...	...

## REFERENCES

- Arce, H. G., Santiago-García, J., Jørgensen, J. K., et al. 2008, *ApJL*, **681**, L21
- Avery, L. W., & Chia, M. 1996, *ApJ*, **463**, 642
- Bachiller, R., & Pérez Gutiérrez, M. 1997, *ApJL*, **487**, L93
- Bachiller, R., Pérez Gutiérrez, M., Kumar, M. S. N., & Tafalla, M. 2001, *A&A*, **372**, 899
- Benedettini, M., Viti, S., Codella, C., et al. 2007, *MNRAS*, **381**, 1127
- Benedettini, M., Viti, S., Codella, C., et al. 2013, *MNRAS*, **436**, 179
- Bergin, E. A., Melnick, G. J., & Neufeld, D. A. 1998, *ApJ*, **499**, 777
- Bolatto, A. D., Wolfire, M., & Leroy, A. K. 2013, *ARA&A*, **51**, 207
- Brown, P. D., Charnley, S. B., & Millar, T. J. 1988, *MNRAS*, **231**, 409
- Ceccarelli, C., Bacmann, A., Boogert, A., et al. 2010, *A&A*, **521**, L22
- Choi, M., Panis, J. F., & Evans, N. J. 1999, *ApJS*, **122**, 519
- Codella, C., Benedettini, M., Beltrán, M. T., et al. 2009, *A&A*, **507**, L25
- Codella, C., Ceccarelli, C., Bottinelli, S., et al. 2012, *ApJL*, **744**, L164
- Codella, C., Lefloch, B., Ceccarelli, C., et al. 2010, *A&A*, **518**, L112
- Corby, J. F., Jones, P. A., Cunningham, M. R., et al. 2015, *MNRAS*, **452**, 3969
- Fontani, F., Codella, C., Lefloch, B., et al. 2014, *ApJL*, **788**, L43
- Garozzo, M., Fulvio, D., Kanuchova, Z., et al. 2010, *A&A*, **509**, A67
- Garrod, R. T. 2013, *ApJ*, **765**, 60
- Garrod, R. T., Widicus Weaver, S. L., & Herbst, E. 2008, *ApJ*, **682**, 283
- Gómez-Ruiz, A. I., Hirano, N., Leurini, S., et al. 2013, *A&A*, **558**, A94
- Gregersen, E. M., Evans, M. J., Zhou, S., et al. 1997, *ApJ*, **484**, 256
- Gueth, F., Guilloteau, S., & Bachiller, R. 1996, *A&A*, **307**, 891
- Gueth, F., Guilloteau, S., & Bachiller, R. 1998, *A&A*, **333**, 287
- Gueth, F., Guilloteau, S., Dutrey, A., et al. 1997, *A&A*, **323**, 943
- Gusdorf, A., Pineau Des Forêts, G., Cabrit, S., et al. 2008, *A&A*, **490**, 695
- Herbst, E., & van Dishoeck, E. F. 2009, *ARA&A*, **47**, 427
- Jiménez-Serra, I., Caselli, P., Martín-Pintado, M., et al. 2008, *A&A*, **482**, 549
- Kwon, W., Fernández-López, M., Stephens, I. W., et al. 2015, *ApJ*, **814**, 43
- Lefloch, B., Cabrit, S., Busquet, G., et al. 2012, *ApJL*, **757**, L25
- Looney, L. W., Tobin, J. J., & Kwon, W. 2007, *ApJ*, **670**, 131
- McGuire, B. A., Carroll, P. B., Dollhopf, N. M., et al. 2015, *ApJ*, **812**, 76
- Mendoza, E., Lefloch, B., López-Sepulcre, A., et al. 2014, *MNRAS*, **445**, 151
- Mikami, H., Umemoto, T., Yamamoto, S., et al. 1992, *ApJL*, **392**, L87
- Müller, H. S. P., Schlöder, F., Stutzki, J., et al. 2005, *JMoSt*, **742**, 215
- Mullins, A. M., Loughnane, R. M., Redman, M. P., et al. 2016, *MNRAS*, **459**, 2882
- Palumbo, M. F. 2015, *BSRSL*, **84**, 33
- Pickett, H. M., Poynter, R. L., Cohen, E. A., et al. 1998, *JQSRT*, **60**, 883
- Podio, L., Lefloch, B., Ceccarelli, C., et al. 2014, *A&A*, **565**, A64
- Quan, D., Herbst, E., Osamura, Y., et al. 2010, *ApJ*, **725**, 2101
- Rawlings, J. M. C., Redman, M. P., Keto, E., et al. 2004, *MNRAS*, **351**, 1054
- Rawlings, J. M. C., Williams, D. A., Viti, S., et al. 2013, *MNRAS*, **430**, 264
- Remijan, A. J., Markwick-Kemper, A., & ALMA Working Group on Spectral Line Frequencies 2007, *BAAS*, **39**, 963
- Requena-Torres, M. A., Martín-Pintado, J., Rodríguez-France, A., et al. 2006, *A&A*, **455**, 971
- Rodríguez-Fernández, N. J., Tafalla, M., Gueth, F., et al. 2010, *A&A*, **516**, A98
- Sault, R. J., Teuben, P. J., & Wright, M. C. H. 1995, in *ASP Conf. Ser. 77, Astronomical Data Analysis Software and Systems IV*, ed. R. A. Shaw, H. E. Payne, & J. J. E. Hayes (San Francisco, CA: ASP), 433
- Tafalla, M., & Bachiller, R. 1995, *ApJL*, **443**, L37
- Tafalla, M., Santiago-García, J., Hacar, A., et al. 2010, *A&A*, **522**, A9
- Takami, M., Karr, J. L., Koh, H., et al. 2010, *ApJ*, **720**, 155
- Van der Tak, F. F. S., Black, J. H., Schöier, F. L., et al. 2007, *A&A*, **468**, 627
- Van Loo, S., Ashmore, I., Caselli, P., et al. 2013, *MNRAS*, **428**, 381
- Viti, S., Codella, C., Benedettini, M., et al. 2004, *MNRAS*, **350**, 1029
- Yamaguchi, T., Takano, S., Watanabe, Y., et al. 2012, *PASJ*, **64**, 105